Available online at www.sciencedirect.com

ScienceDirect

Energy Procedia 148 (2018) 924–931

Energy Procedia

www.elsevier.com/locate/procedia

73rd Conference of the Italian Thermal Machines Engineering Association (ATI 2018), 12-14 September 2018, Pisa, Italy

Mode decomposition methods for the analysis of cavitating flows in turbomachinery

Maria Grazia De Giorgi[a,*], Antonio Ficarella[a], Donato Fontanarosa[a]

[a]*University of Salento, Dep. of Engineering for Innovation, Via per Monteroni, 73100-Lecce, Italy*

Abstract

The present work is aimed at the characterization of the cavitating flow regimes by applying the coupled POD/DMD technique to the vapor volume fraction field. The proposed approach provided an improved spatio-temporal-frequency description of the flow, based on the detection of the most energetic flow structures with information about their shape and size, and their decomposition into wave patterns oscillating with specific frequency and decay rate. The novel technique was applied to numerical results concerning the bubble cavitation and the supercavitation regimes of 2D water flows around a NACA hydrofoil at ambient temperature. Numerical simulations were performed by using a homogenous mixture model equipped with an extended Schnerr-Sauer cavitation model, in combination with a Volume of Fluid (VOF) interface tracking method.

The proposed approached provided a better characterization of the unsteady cavitating flow, and allowed for a deeper insight about the dynamics of the vapor cavity, especially in cases involving the more chaotic regime of supercavitation. In particular, POD results figured out the most energetic coherent vapor structures associated to each cavitation regime: the first mode highlighted the main sheet cavity which grew on the hydrofoil up to detached, the second mode pointed out the cavitating/condensating doublet structures and the third mode figured out the smaller structures owning less energy but a higher frequency content. DMD modes performed a decomposition of the coherent structures detected by means of the POD analysis, into a subset of vapor pattern periodically evolving with a single frequency and a characteristic decay rate. Furthermore, results showed that the supercavitating flow structures owned characteristic frequencies which ranged from 5 to 26 Hz, while the less intensive bubble cavitation regime was characterized by frequencies ranging from 15 to 42 Hz.

Keywords: unsteady cavitation; fluid induced instabilities; cavitation regimes; Proper Orthogonal Decomposition; Dynamic Mode Decomposition; Computational Fluid Dynamics

*Corresponding author. Address: University of Salento, Dept. of Engineering for Innovation, Research Center for Energy and Environment (UNISALENTO-DII-CREA), Via per Monteroni, LECCE I-73100, Italy. Tel: +39 0832297759.

E-mail address: mariagrazia.degiorgi@unisalento.it

10.1016/j.egypro.2018.08.093

1. Introduction

In the last years, the interest in modal decomposition techniques has increased and nowadays they are considered an important tool of choice for data-driven analysis of non-linear flows. Generally, a modal decomposition takes a set of data and from it computes a set of modes, or characteristic features. In the field of cavitating flows, Watanabe et al. [1] investigated the properties of unsteady structures of cavitating water-jet using a combination of shadowgraph imaging with POD analysis. Recently, Jiri et al. [2] implemented a POD analysis to investigate the dynamics of cavitation within a venturi nozzle during the transition from fully developed cavitation to supercavitation regime. Instead, De Giorgi et al. [3] applied the POD to characterizing the cavitating flow regimes inside a sharp-edged cylindrical orifice. The application of the POD for a modal analysis of the cavitating flows over hydrofoils was experienced by Prothin et al. [4]. Recently, Wang et al. [5] applied the POD in order to characterize the coherent large-scale flow unsteadiness of velocity fields in case of ventilated cavitation. However, the POD modes does not provide clear information about the frequency content of the detected coherent structures. In this regard, the Dynamic Mode Decomposition (DMD) is able to provide a spatio-frequency characterization of the cavitating flow. In the field of the fluid dynamics, the DMD technique has been initially applied by [6] to a plane channel flow, a flow over a two-dimensional cavity, the wake flow behind a flexible membrane and a jet passing between two cylinders. Recently, Wen et al. [7] characterized the different fluctuating behaviors of the jet flow due to the different jet shapes by Lagrangian dynamic mode decomposition (DMD). Concerning cavitating flows, Prothin et al. [8] experimentally studied the spatial and temporal behavior of the vapor cavity when it develops on the same foil at high Reynolds number by using the POD in combination with the DMD.

The present work is aimed to provide an improved spatio-temporal-frequency characterization of unsteady cavitating flows in turbomachineries, by using the snapshot POD in combination with DMD. By means of a combined approach, the most energetic flow structures were detected by means of the POD with information about their shape and size, while the DMD provided a decomposition of the most energetic coherent structures into wave patterns oscillating with specific frequency and decay rate. In particular, the main Fast Fourier Transform frequencies of POD modes were related to the corresponding DMD frequencies and its vapor patterns. The coupled POD/DMD methodology was applied to the liquid volume fraction field α_l resulting from 2D computational fluid dynamics (CFD) simulations of a water flow around a NACA 0015 foil at ambient temperature and different cavitation conditions. An extended Schnerr-Sauer cavitation model which took account of thermal effects and the latent heat was used for CFD computations.

2. Coupled Proper Orthogonal Decomposition/Dynamic Mode Decomposition (POD/DMD)

POD analysis extracts an orthogonal basis of eigenvalues, related to the modes of the flow data field $u(\mathbf{x};t)$. N_t is the number of time steps considered over a spatial domain of M grid points. Then spatial and temporal contributions are decoupled obtaining two different *eigenfunctions*. These eigenfunctions are characteristic of the most probable realizations of the input data and they represent the energy stored in them. Practically, POD results in $u(\mathbf{x};t) = \sum_i u_i(\mathbf{x};t) = \sum_i a_i(t)\phi_i(\mathbf{x})$, where $\phi_i(\mathbf{x})$ represents the i-th spatial eigenfunction, also called *eigenface*, which consists of a picture of the flow able to capture the scales and shapes of its modal coherent structures. $a_i(t)$ is the i-th temporal eigenfunction, and collect information about the dynamics of the corresponding modal coherent structure. In the present work the snapshot method [9] was used, which is based on the spatial averaging and the temporal correlation of the sequence of the flow field dataset, so as to result to be suitable when the data field has a good spatial resolution but a relatively short time history. By using this approach the size of the eigenvalue problem becomes $N_{POD} = N_t$, and the energy contribution in image reconstruction related to the j-th POD mode is defined as $\Lambda_j = (\lambda_j)/(\sum_{k=1}^{N_{POD}} \lambda_k)$, where λ_i is the i-th eigenvalue of the autocorrelation tensor of the flow field data.

An extended description of the POD technique was provided by Tropea [10], who demonstrated that it is a robust decomposition technique in an energetic sense. However, it losses important information about the dynamics of the flow such as the frequency content associated to each mode. In this regards, the Dynamic Mode Decomposition (DMD) [11, 6, 12] decomposes the given dataset into modal spatial coherent structures, or wave patterns, and the corresponding oscillatory modes consisting in a single oscillation frequency and a characteristic decay rate. In particular,

given the same snapshots of N_t experimental or numerical observations of the flow field $u(\mathbf{x}, t) = u_i(\mathbf{x})$ of size M, it is supposed there exists a Koopman-like linear operator [13] $K \in \mathbb{C}^{M \cdot N_T}$, which defines the temporal evolution of the flow field as $u_i(\mathbf{x}) = K\ u_{i+1}(\mathbf{x})$ Hence, based on the Singular Value Decomposition (SVD) algorithm, the reconstruction of the k-th snapshot is obtained as $u_k(\mathbf{x}) = \sum_{i=1}^{N_t} \left(\lambda_i^{DMD}\right)^k \phi_i^{DMD}$, where $\lambda_i^{DMD} \in \mathbb{C}$ is the i-th eigenvalue of the matrix derived by SVD, and ϕ_i^{DMD} is the i-th DMD mode, a.k.a. dynamic mode. In particular, $\lambda_i^{DMD} \in \mathbb{C}$ contains information about the modal frequency $\angle\lambda_i^{DMD}$ and the decay rate $\left\|\lambda_i^{DMD}\right\|$.

Contrary to the POD, in DMD there is no natural way to rank the contributions of the different DMD modes. Moreover, the modes are not orthogonal what further complicated the choice. Thus, the most relevant DMD modes have been selected by considering the modal frequencies extracted from FFT computations of the temporal POD eigenfunction $a_i(t)$, and then comparing the corresponding DMD and POD eigenstructures.

3. Numerical approach

Numerical simulations were performed by using the open source CFD toolbox OpenFOAM© Version 3.0.1, based on a Finite Volume formulation. Based on the formulation previously proposed by De Giorgi et al. [14], a homogeneous mixture/mass transfer model was used in combination with an extended Schnerr-Sauer cavitation model for the computation of the mass transfer rates of evaporation. An Antoine-like equation relates saturation conditions to the local conditions, so as to introduce the dependence of the saturation pressure to the local temperature $p_{sat}(T)$. The vapor pressure $p_{vap}(T)$ is derived from the saturation pressure $p_{sat}(T)$ as $p_{vap}(T) = p_{sat}(T) + p_{turb}/2$, where p_{turb} is the correction related to the turbulent pressure fluctuations [15]. A nuclation vapor volume fraction α_{NUC} initializes the cavitation process as $\alpha_{NUC} = (\frac{\pi d_{NUC}^3 n_b}{6})/(1 + \frac{\pi d_{NUC}^3 n_b}{6})$, where n_b and d_{NUC} respectively represent the density of the nucleation sites and the nuclei diameter and n_b. Instead, the radius of the vapor bubble R_b is computed from the definition of the vapor and liquid volume fractions, $alpha_{vapor}$ and α_l, as $\alpha_{vapor} = 1 + \alpha_{NUC} - \alpha_l = (\frac{4}{3}\pi R_b^3 n_b)/(1 + \frac{4}{3}\pi R_b^3 n_b)$.

Thermal effects takes account of the latent heat of phase change, while the convective heat transfer was neglected due to the small temperature drop inside the vapor bubble. The heat transfer consists in the latent heat source term, computed as $\dot{Q} = R\ h_L$ where h_L is the latent heat of vaporization.

4. Test cases and numerical setup

A water flow around the NACA 0015 hydrofoil was investigated at at an angle of attack (AoA) equal 8° and 298 K as in [16]. The cavitation condition was defined by the cavitation number σ The bubble cavitation regime at $\sigma = 2.1$ and the supercavitation regime at $\sigma = 1.2$ were investigated. The computational domain is shown in Fig. 1(a) and (b). It extended $3c$ upstream of the leading edge and $5c$ downstream of the trailing edge of the hydrofoil, and the chord of the hydrofoil is 0.115 m. The flow was confined in a rectangular duct having an height of 0.12 m.

Unsteady simulations started from a steady-state non-cavitating solution, obtained by applying the Semi-Implicit Method for Pressure Linked Equations (SIMPLE) algorithm. Instead, the unsteady cavitating flow was solved based on the PIMPLE algorithm [17], while the Multidimensional Universal Limiter for Explicit Solution (MULES) algorithm [18] was used in order to compute the field of the liquid volume fraction. A number of 35 iterations were set into the PIMPLE algorithm in combination with residual tolerances of 1×10^{-5} for the static pressure and 1×10^{-6} for the velocity and the turbulent quantities. Time derivatives were computed with the first order, bounded and implicit Euler scheme. The following numerical schemes were used in reference to the convective fluxes: the Self Filtered Central Differencing (SFCD) scheme for the velocity field, the van Leer scheme for the volume fraction of liquid, the Gauss upwind scheme for the temperature, and the linear upwind differencing scheme for all remaining fields. The gradient and the Laplacian of all fields were computed by means of the least squares scheme and the Gauss linear scheme respectively. A linear scheme was used for interpolations. The Density Correction Model (DCM) by [19] was implemented inside the $k - \omega$-Shear Stress Transport model (SST) by [20]. Consequently, the turbulent viscosity was modified by replacing ρ with the correction function $f(\rho) = \rho_v + \alpha^{10}(\rho_l - \rho_v)$. Concerning the boundary conditions, the no-slip condition was imposed on the hydrofoil, as well as on the upper and bottom walls. In addition, the velocity of the flow was fixed at $4\ \mathrm{m\,s^{-1}}$, which corresponds to a Reynolds number equal to 5.14×10^5. The outlet pressure was

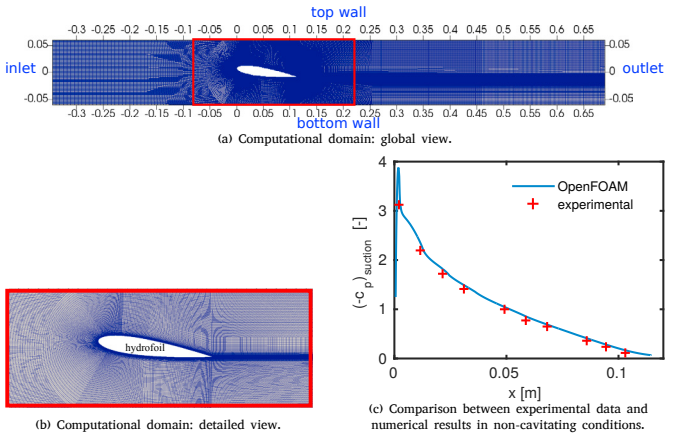

(a) Computational domain: global view.

(b) Computational domain: detailed view.

(c) Comparison between experimental data and numerical results in non-cavitating conditions.

Fig. 1: Computational domain: (a) global representation of the mesh and boundaries; (b) detailed view of the mesh close to the hydrofoil; (c) Comparison of the pressure coefficient C_p between the numerical results and experimental data [16].

derived from the cavitation number σ. The initial temperature field was set to 298 K. The water flow was simulated by using a fixed time step of 1×10^{-4} s, and each unsteady simulation was stopped at $t = 0.9$ s.

Based on steady-state computations in non cavitating conditions at $\sigma = 5$, a grid dependency study (GIS) was performed based on three meshes, differently refined close to the hydrofoil surface. The GIS led to the choice of a mesh composed of 93172 cells and characterized by a max imum y^+ equal to 2.01, which provided the best trade-off between accuracy and computational cost. Fig. 1(c) shows the comparison between experiments [16] and CFD results of the pressure coefficient of the suction side in non-cavitating condition obtained on the selected mesh.

5. Results and discussion

The present work focused on the spatio-temporal-frequency characterization of the dynamics of the cavity by applying the combination of POD and DMD mode decomposition techniques. In particular, the POD was applied to the temporal series of the fluctuations of α_l, i.e. $\alpha_l' = \alpha_l - \alpha_{l,avg}$. On the contrary, the DMD was directly applied to α_l, without mean subtraction.

For each cavitating flow regime the map of the average liquid volume fraction $\alpha_{l,avg}$ (see Figg. 2(a) and (b)) was first constructed. Hence, the mean dimensionless cavity length L_{cav}/c was estimated based on thresholding on $\alpha_{l,avg}$

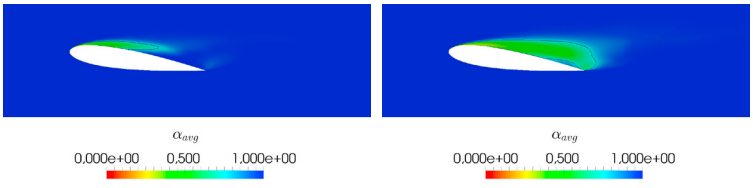

(a) $\sigma = 2.1$ (b) $\sigma = 1.2$

Fig. 2: Average liquid volume fraction α_{avg}, at $\sigma = 2.1$ ((a) and (c)) and $\sigma = 1.2$ ((b) and (d)).

at 0.75, in the same way as experimentally predicted by [16]. As reported in Tab 1, the numerical estimation of L_{cav}/c well agreed the experimental ones, especially in case of bubble cavitation (SIM1). Concerning the supercavitation regime (SIM2), CFD computations well predicted the supercavitation condition $L_{cav}/c > 1$, albeit they led to an underestimation of L_{cav}/c. In combination with the map of $\alpha_{l,avg}$, it was found that the lower the cavitation number is, the more extended the high frequency region results, even though with smaller frequency and long-lasting vapor structures.

The modal characterization started by applying the snapshot Proper Orthogonal Decomposition (POD) which allowed for the detection of the most energetic coherent vapor structures. At the beginning, a convergence test on

Table 1: Dimensionless cavity lengths L_{cav}/c, and relative energies of POD modes 1-3.

Test Case	σ	**Cavitation regime**	$\alpha_{\mathbf{l,avg}}$**-thresholding** $\bar{\alpha}_{thres} = 0.75$	**Experimental Cervone et al. [16]**	$\mathbf{\Lambda_1}$ [%]	$\mathbf{\Lambda_2}$ [%]	$\mathbf{\Lambda_3}$ [%]
SIM1	2.1	bubble cavitation	0.658	$0.536^{+0.249}_{-0.160}$	54.2	13	5.6
SIM2	1.2	supercavitation	1.086	$1.294^{+0.065}_{-0.065}$	34	18.3	10.3

the relative energy of the main POD modes confirmed that the available number of snapshot $N_t = 900$ ensured the convergence of POD computations. The relative energies of modes 1-3 in case of bubble cavitation (SIM1) and supercavitation (SIM2) are reported in Tab. 1. It resulted that the energy of the first mode decreased as the supercavitation condition was approached. Instead, the second and the third modes confirmed that the relevance of the less energetic structures increased as σ reduced. Figure 3 shows the topography of the coherent cavitating structures referred to POD modes 1-3 at $\sigma = 2.1$ and 1.2. In general, the first mode revealed the sheet cavity attached to the hydrofoil which

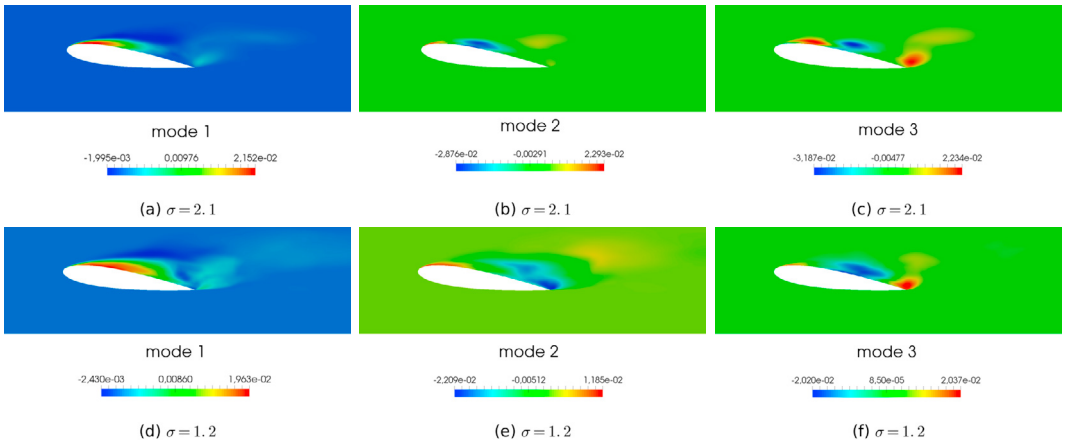

Fig. 3: POD eigenstructures: (a) $\sigma = 2.1$, mode 1; (b) $\sigma = 2.1$, mode 2; (c) $\sigma = 2.1$, mode 3; (d) $\sigma = 1.2$, mode 1; (e) $\sigma = 1.2$, mode 2; (f) $\sigma = 1.2$, mode 3.

grew from leading edge up to the detachment due to the re-entrant jet, as evinced by comparing Fig. 3(a) and (d). The second modes (Fig. 3(b) and (d)) highlighted two structures having opposite sign: this means that when the one grew due to cavitation, the other one collapsed due to transport and/or condensation. In particular, supercavitation exhibited a larger structure toward the trailing edge related to the the vapor cloud which formed after the complete detachment of the sheet cavity. At the same time, a smaller structure was placed at the leading edge which is probably related to the growth mechanism of the new vapor cavity after the collapse of the detached cloud. The two structures were close to each other during bubble cavitation, pointing out the dynamics of the bubble detachment and collapse again. The third modes (Fig. 3(c) and (d)) retrieved the smaller structures owining a shorter lifetime and less energy. During supercavitation these structures were still relevant, highlighting the second vapor structure formed at the trailing edge and the breaking jet caused by the liquid entrainment close to the hydrofoil owing to the rapid growth of the sheet cavity.

Due to the limitation of POD in characterizing the dynamics in the frequency domain, it was coupled with the application of the Dynamic Mode Decomposition to the same dataset of α_l based on the Fast Fourier Transform (FFT) analysis of the temporal POD eigenfunctions $a_i(t)$ of modes 1-3. In particular, the FFT analysis led to the individuation of three characteristic frequencies for each mode, as shown in Fig. 4. Hence, DMD computations provided a single eigenstructure to each characteristic frequency, so as to obtain a decomposition of the most energetic coherent structures detected by POD computations which owned a more complex dynamics, into a subset of cavitation patterns characterized by a single pure frequency and a decay rate. Results of DMD computations are reported in Fig. 5 and 6 for bubble cavitation and supercavitation respectively, as well as in Tab. 2.

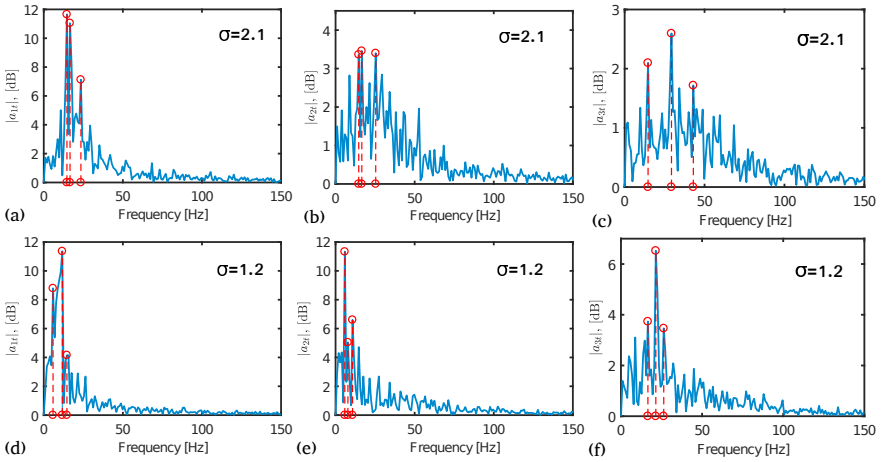

Fig. 4: FFT spectra of temporal POD eigenfunctions $a_i(t)$: (a) $\sigma = 2.1$, mode 1; (b) $\sigma = 2.1$, mode 2; (c) $\sigma = 2.1$, mode 3; (d) $\sigma = 1.2$, mode 1; (e) $\sigma = 1.2$, mode 2; (f) $\sigma = 1.2$, mode 3.

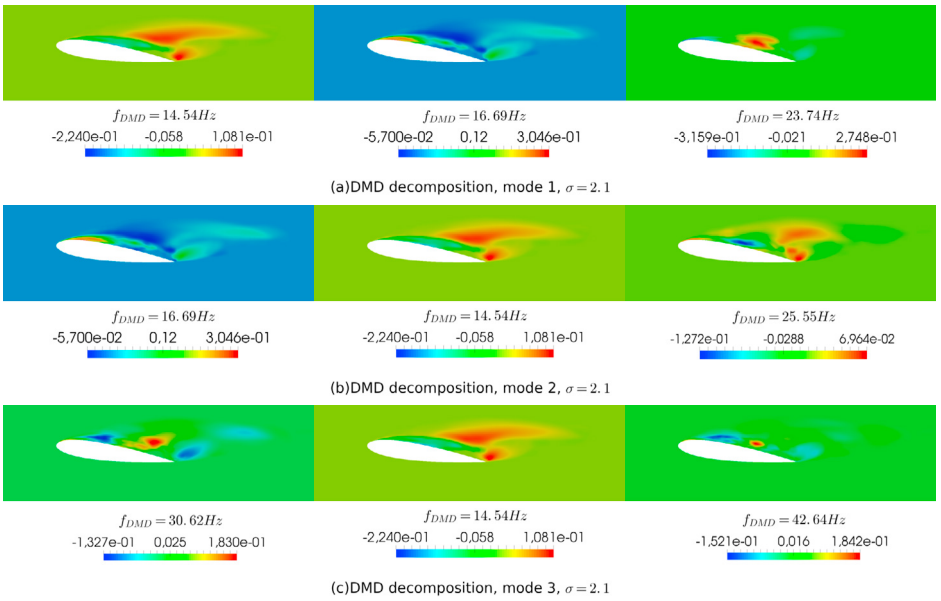

Fig. 5: DMD eigenstructures at $\sigma = 2.1$: (a) related to POD mode 1; (b) related to POD mode 2; (c) related to POD mode 3.

As highlighted in Fig. 4(a), during bubble cavitation POD mode 1 exhibited two characteristic frequencies of about 15 Hz with similar amplitudes, and a third one which owned less energy. The DMD modes in Fig. 5(a) highlighted that these frequencies are related to vapor structure with similar shape corresponding to the sheet cavity pictured in Fig. 3(a). Instead, POD mode 2 evolved with three frequencies which had almost the same amplitude (see Fig. 4(b), and DMD modes in Fig. 5(b) decomposed the doublet structure in Fig. 3(b) into two substructures evolving with different frequencies: the cavitating structure which formed at 15 Hz, and the detached vapor structure which was condensing at approximately 25 Hz. This results highlighted that the vapor cavity dynamics exhibited evaporation and the condensation processes with different characteristic times. The third POD mode owned less energy but showed high frequency content (see Fig. 4(c)) up to approximately 42 Hz, and the DMD modes in Fig. 5(c) confirmed that they are related to the dynamic of small structures which oscillates with a reduced energy content and lifetime, yet with a greater frequency. During supercavitatioon, the main sheet cavity structure of Fig. 3(d) and the doublet cavitating/condensating structures evinced in Fig. 3(e) were retrieved and dynamically characterized by means of the modal

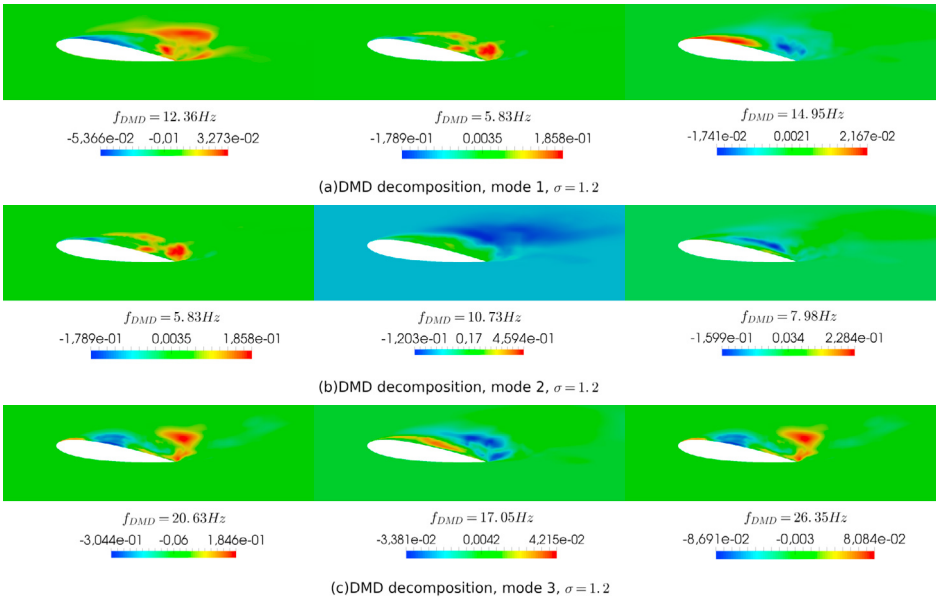

Fig. 6: DMD eigenstructures at $\sigma = 1.2$: (a) related to POD mode 1; (b) related to POD mode 2; (c) related to POD mode 3.

Table 2: DMD frequencies f_{DMD} and the corresponding decay rates $\left\|\lambda_i^{DMD}\right\|$.

σ	$\mathbf{f_{DMD}}$ [Hz]	$\left\|\lambda_\mathbf{i}^\mathbf{DMD}\right\|$ [-]	σ	$\mathbf{f_{DMD}}$ [Hz]	$\left\|\lambda_\mathbf{i}^\mathbf{DMD}\right\|$ [-]
2.1	14.54	0.9992	1.2	5.83	0.9971
2.1	16.69	0.9976	1.2	7.98	0.9980
2.1	23.74	0.9942	1.2	10.73	0.9979
2.1	25.55	0.9986	1.2	12.36	1.0009
2.1	30.62	0.9963	1.2	14.95	1.0027
2.1	42.64	0.9959	1.2	17.05	1.0009
			1.2	20.63	0.9979
			1.2	26.35	0.9994

eigenstructures showed in Fig. 6(a) and (b). With respect to the bubble cavitation regime, POD mode 1 and 2 had similar energies and consequently exhibited similar frequencies in the range 5 – 15Hz. In general, the lower the cavitation number resulted in a slower the shedding dynamics, which was confirmed by considering the third POD mode (see Fig. 4(e)). In particular, the DMD modes of Fig. 6(c) highlighted that the vapor cloud dynamics at the trailing edge had frequencies ranging between 20 and 26 Hz, while the dynamics of the liquid entrainment due to a rapid growth of the main cavity took place approximately at 17 Hz.

At the end, the present work demonstrated that the coupling between the POD and DMD techniques provided important benefits in the study of unsteady cavitating flows, allowing for a deeper insight about the dynamics of the vapor cavity, especially in cases involving such chaotic regimes as supercavitation. In particular, the improved spatio-temporal-frequency description of the vapor cavity structures can support the definition of the mass flow gain factor and the internal compliance of cavitating turbopumps, which describe the influence of the fluctuations of the mass flow rate and the pressure at inlet associated with the variation of the vapor cavity volume. They are the key factors for the stability of the pumping system with respect to the establishment of the two major instabilities, namely the rotating cavitation and the cavitation surge. Furthermore, the modal decomposition of the flow dynamics would allow for a better investigation of the nonlinear effects of cavitation, distinguishing the largest/slower and most detrimental vapor structures, to the smaller ones which introduce higher destabilizing natural frequencies.

6. Final remarks

The present work provided a spatio-temporal-frequency characterization of cavitating flows of water around a NACA 0015 hydrofoil, by using the snapshot Propert Orthogonal Decomposition (POD) in combination with the Dynamic Mode Decomposition (DMD). The characterization concerned the liquid volume fraction field α_l resulting from 2D computational fluid dynamics (CFD) simulations in accordance with the experimental work by [16]. An extended Schnerr-Sauer cavitation model which took account of thermal effects and the latent heat was used for CFD computations. The coupling between POD and DMD consisted in detecting the main Fast Fourier Frequency of POD modes which were related to the corresponding DMD frequency and its vapor pattern. Both bubble cavitation regime and supercavitation were investigated. The first POD mode highlighted the main sheet cavity which grew on the hydrofoil up to detached. Instead, the second POD mode pointed out the cavitating/condensating doublet structures and the third POD mode figured out the smaller structures owning less energy but a higher frequency content. DMD modes performed a decomposition of the coherent structures detected by means of the POD analysis, into a subset of vapor pattern periodically evolving with a single frequency and a characteristic decay rate. Furthermore, results showed that the supercavitating flow structures owned characteristic frequencies which ranged from 5 to 26 Hz, while the less intensive bubble cavitation regime was characterized by frequencies ranging from 15 to 42 Hz.

References

[1] R. Watanabe, T. Kikuchi, T. Yamagata, N. Fujisawa, Shadowgraph imaging of cavitating jet, Journal of Flow Control, Measurement & Visualization 3 (03) (2015) 106.

[2] K. Jiri, R. Pavel, H. Rostislav, H. Martin, C. Radomir, U. Ondrej, M. Blahoslav, M. EliÅka, P. FrantiÅek, Å. David, Transition of cavitating flow to supercavitation within venturi nozzle - hysteresis investigation, in: EPJ Web of Conferences, Vol. 143, 2017. doi:10.1051/epjconf/201714302055.

[3] M. De Giorgi, D. Fontanarosa, A. Ficarella, Characterization of cavitating flow regimes in an internal sharp-edged orifice by means of proper orthogonal decomposition, Experimental Thermal and Fluid Science 93 (2018) 242 – 256. doi:https://doi.org/10.1016/j.expthermflusci.2018.01.001.

[4] S. Prothin, H. Djeridi, J.-Y. Billard, Coherent and turbulent process analysis of the effects of a longitudinal vortex on boundary layer detachment on a naca0015 foil, Journal of Fluids and Structures 47 (2014) 2–20. doi:10.1016/j.jfluidstructs.2013.08.014.

[5] Z. Wang, B. Huang, M. Zhang, G. Wang, X. Zhao, Experimental and numerical investigation of ventilated cavitating flow structures with special emphasis on vortex shedding dynamics, International Journal of Multiphase Flow 98 (2018) 79 – 95. doi:https://doi.org/10.1016/j.ijmultiphaseflow.2017.08.014.

[6] P. J. Schmid, Dynamic mode decomposition of numerical and experimental data, Journal of fluid mechanics 656 (2010) 5–28.

[7] X. Wen, Y. Liu, H. Tang, Unsteady behavior of a sweeping impinging jet: Time-resolved particle image velocimetry measurements, Experimental Thermal and Fluid Science 96 (2018) 111–127. doi:10.1016/j.expthermflusci.2018.02.033.

[8] S. Prothin, J.-Y. Billard, H. Djeridi, Image processing using proper orthogonal and dynamic mode decompositions for the study of cavitation developing on a naca0015 foil, Experiments in Fluids 57 (10). doi:10.1007/s00348-016-2246-1.

[9] L. Sirovich, Turbulence and the dynamics of coherent structures. i. coherent structures, Quarterly of applied mathematics 45 (3) (1987) 561–571.

[10] C. Tropea, A. L. Yarin, J. F. Foss, Springer handbook of experimental fluid mechanics, Vol. 1, Springer Science & Business Media, 2007.

[11] C. W. ROWLEY, I. MEZI, S. BAGHERI, P. SCHLATTER, D. S. HENNINGSON, Spectral analysis of nonlinear flows, Journal of Fluid Mechanics 641 (2009) 115127. doi:10.1017/S0022112009992059.

[12] J. H. Tu, C. W. Rowley, D. M. Luchtenburg, S. L. Brunton, J. N. Kutz, On dynamic mode decomposition: theory and applications, arXiv preprint arXiv:1312.0041.

[13] I. Mezić, Spectral properties of dynamical systems, model reduction and decompositions, Nonlinear Dynamics 41 (1) (2005) 309–325. doi:10.1007/s11071-005-2824-x.

[14] M. De Giorgi, A. Ficarella, D. Fontanarosa, Implementation and validation of an extended schnerr-sauer cavitation model for non-isothermal flows in openfoam, in: Energy Procedia, Vol. 126, 2017, pp. 58–65. doi:10.1016/j.egypro.2017.08.057.

[15] A. K. Singhal, M. M. Athavale, H. Li, Y. Jiang, Mathematical basis and validation of the full cavitation model, Transactions-American Society of Mechanical Engineers Journal of Fluids Engineering 124 (3) (2002) 617–624.

[16] A. Cervone, C. Bramanti, E. Rapposelli, L. D'Agostino, Thermal cavitation experiments on a naca 0015 hydrofoil, Journal of Fluids Engineering, Transactions of the ASME 128 (2) (2006) 326–331. doi:10.1115/1.2169808.

[17] T. Holzmann, Mathematics, numerics, derivations and openfoam®.

[18] E. Krepper, D. Lucas, T. Frank, H.-M. Prasser, P. J. Zwart, The inhomogeneous musig model for the simulation of polydispersed flows, Nuclear Engineering and Design 238 (7) (2008) 1690 – 1702. doi:https://doi.org/10.1016/j.nucengdes.2008.01.004.

[19] J.-L. Reboud, B. Stutz, O. Coutier-Delgosha, Two-phase flow structure of cavitation: Experiment and modeling of unsteady effects, 3rd International Symposium on Cavitation (CAV1998), Grenoble, France (1998) (10 1998).

[20] F. R. Menter, Two-equation eddy-viscosity turbulence models for engineering applications, AIAA journal 32 (8) (1994) 1598–1605.